


Nonlocal Scatterer for Compact Wave-Based Analog Computing

Heedong Goh^{1,2} and Andrea Alù^{1,2,3,*}

¹*Department of Electrical and Computer Engineering, The University of Texas at Austin, Austin, Texas 78712, USA*

²*Photonics Initiative, Advanced Science Research Center, City University of New York, New York, New York 10031, USA*

³*Physics Program, Graduate Center, City University of New York, New York, New York 10016, USA*

 (Received 10 March 2021; accepted 25 January 2022; published 18 February 2022)

Analog computing based on wave interactions with metamaterials has been raising significant interest as a low-energy, ultrafast platform to process large amounts of data. Engineered materials can be tailored to impart mathematical operations of choice on the spatial distribution of the impinging signals, but they also require extended footprints and precise large-area fabrication, which may hinder their practical applicability. Here we show that the nonlocal response of a compact scatterer can be engineered to impart operations of choice on arbitrary impinging waves, and even to solve integro-differential equations, whose solution is observed in the scattered fields. The lack of strongly resonant phenomena makes the response robust, and the compact nature opens to scalability and cascading of these processes, paving the way to efficient, compact analog computers based on engineered microstructures.

DOI: 10.1103/PhysRevLett.128.073201

Demands for fast and energy-efficient computation and data processing have been driving to saturation the progress in digital computing. These challenges have been reviving the interest in wave-based analog computing based on metamaterials, which offer the possibility to impart mathematical operations of choice on the spatial distribution of arbitrary impinging signals [1–5]. These opportunities allow real-time, massively parallel computations on large images or sets of data with minimal energy requirements. Based on this approach, several optical and acoustic metamaterial devices have been designed to perform differentiation and integration [1–12] and, by adding feedback to the wave interactions in these materials, it is possible to realize analog equation solvers [13–16] and recurrent neural networks [17].

The basic principle underlying these concepts is that a target linear mathematical operation on the spatial (temporal) variations of a physical quantity of interest can be described as a kernel operating on the momentum (frequency) spectrum of the metamaterial response. By tailoring large-area metamaterials or metasurfaces, and controlling a large set of resonant elements and their mutual interactions, it is possible to imprint this kernel into a practical structure. In this Letter, we show that it is possible to realize wave-based analog computation in its most compact form based on engineering the nonlocality of a single compact scatterer. To enable a complex mathematical operation in a small form factor, we engineer the nonlocality of its scattering response in order to map a kernel of choice into the manipulation of the discrete spectrum of wave harmonics composing its scattering response. We use inverse design [15,18–25] to optimize the nonlocality, enabling an efficient and robust operation as a compact analog computer.

In order to keep the formulation scalar, we focus on a two-dimensional object of limited size excited by a transverse-magnetic wave, as shown in Fig. 1. The scattering problem is governed by the wave equation

$$\left(\text{div grad} + \varepsilon \frac{\omega^2}{c^2}\right)E(r, \theta) = 0, \quad (1)$$

where E is the total electric field normal to the plane, ω is the angular frequency, c is the wave speed in vacuum, ε is the relative permittivity, and (r, θ) are the cylindrical coordinates centered with the object of interest. Small scatterers typically interact with the incoming waves

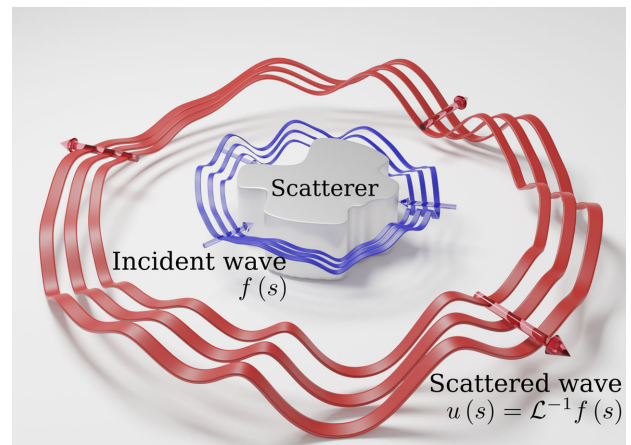


FIG. 1. A nonlocal scatterer for wave-based analog computing. A source function $f(s)$ modulates the incident fields; the solution $u(s) = \mathcal{L}^{-1}f(s)$ is obtained by measuring the scattered (outgoing) fields around the scatterer.

through a local response [26], which implies that the local electric field at the center of the scatterer induces a monopole associated with the zeroth-order outgoing cylindrical harmonic, the first derivatives of the electric field distribution induce electric dipoles associated with the first-order cylindrical harmonics, and so on. However, by controlling the geometry of the scatterer, it is possible to engineer a much more complex, nonlocal response of choice, based on which these quantities are coupled together by design. We can generally define the scattering matrix \mathbf{S} according to a certain choice of basis functions that expands impinging and scattered waves:

$$\mathbf{d}^+ = \mathbf{S} \cdot \mathbf{d}^-, \quad (2)$$

where \mathbf{d}^- is the coefficient vector describing the impinging wave E^- and \mathbf{d}^+ describes the scattered wave E^+ , such that $E = E^- + E^+$ satisfies Eq. (1). For example, we can expand the impinging wave using Hankel functions of the second kind $H_n^{(2)}$, representing converging waves, and the scattered wave using Hankel functions of the first kind $H_n^{(1)}$, representing diverging waves:

$$\begin{aligned} E^-(r, \theta) &= \sum_{n \in \mathbb{Z}} d_n^- e^{im\theta} H_n^{(2)}(kr) \quad \text{and} \\ E^+(r, \theta) &= \sum_{n \in \mathbb{Z}} d_n^+ e^{im\theta} H_n^{(1)}(kr), \end{aligned} \quad (3)$$

under an $e^{-i\omega t}$ time dependence. Here, i is the imaginary unit and $k = \omega/c$ is the free-space wave number. We note that the above expansion in cylindrical harmonics describes the wave fields outside of the scatterer, hence it does not include the singularity of Hankel functions at the origin, ensuring that this formulation is well behaved anywhere in the relevant domain. Other field expansions, for instance, involving Bessel functions, are also possible without affecting the general formulation described in the following, as discussed in more detail in the Supplemental Material [27].

A local scatterer is characterized by a diagonal matrix \mathbf{S} , in which each cylindrical harmonic scatters only into the same order. However, suitably tailored scatterer geometries can support engineered nonlocality that couples the various scattering orders at will, and in general \mathbf{S} can be a fully populated matrix. The microstructure of the scatterer can control each element of the scattering matrix within the constraints dictated by reciprocity and power conservation, engineering the scatterer nonlocality by controlling the coupling among the relevant scattering harmonics. The recent interest in large Willis coupling in acoustic scatterers [28–30] is a basic example of how engineered microstructures can control the nonlocal response of compact scatterers and correspondingly tailor the coupling among orthogonal scattering harmonics, even though limited only

to the first two harmonics. In this Letter, we extend this paradigm to a much wider control over the nonlocal coupling among several scattering harmonics to enable wave-based analog computing.

In order to show what is possible through engineered nonlocal scatterers in the context of analog computing, we consider the solution of the general linear equation

$$\mathcal{L}(s)[u(s)] = f(s), \quad (4)$$

where \mathcal{L} is an arbitrary linear operator, f is an input function, u is the unknown function, and s is the argument of the problem. We aim at demonstrating that a suitably tailored scatterer can map the solution $u = \mathcal{L}^{-1}f$ into the scattered fields at a user-defined observation contour when it is interrogated with an impinging wave corresponding to the input function f , as schematically sketched in Fig. 1. As observation contour, we choose a circumference surrounding the object, mapping the variable $s \in (0, 2\pi)$ onto the angle θ . Our input function f is mapped in the scattering problem into a superposition E^+ of converging scattering harmonics, the kernel operator \mathcal{L} is imprinted into the nonlocal scatterer by tailoring its scattering matrix \mathbf{S} , so that the diverging scattered fields E^- represent the solution $u = \mathcal{L}^{-1}f$.

For a given scatterer size, a finite number $2N + 1$ of cylindrical harmonics contributes to the overall scattering response, with a rule of thumb $N \sim ka$, where a is the circumference enclosing the object [26]. For the given mathematical problem of interest, as in Eq. (3), we choose the scatterer size so that it interacts with a sufficient number of scattering harmonics that can approximate the operator \mathcal{L} and input function f of interest with a truncated series of $2N + 1$ harmonics. We start with a weak form of Eq. (4), which reads

$$\int_0^{2\pi} v(\mathcal{L}u - f)ds = 0, \quad \forall v \in \mathcal{V}, \quad (5)$$

where v is a test function and \mathcal{V} is the corresponding vector space. By taking finite-dimensional approximations such that $v \approx v^h$ and $u \approx u^h$, we obtain [27]

$$\begin{aligned} v^h(s) &= \sum_{m=-N}^N v_m e^{-ims} \left[2\pi H_m^{(2)}(kr_o) \right]^{-1} \quad \text{and} \\ u^h(s) &= \sum_{n=-N}^N u_n e^{ins} H_n^{(1)}(kr_o), \end{aligned} \quad (6)$$

where r_o is the radius of an arbitrary circular contour over which we sample the scattering pattern to measure our output. This formulation expands f into a finite series of cylindrical harmonics representing our input, and u in a series of diverging harmonics, which represent our desired solution. By plugging this result into (5), we approximate

the infinite-dimensional linear equation (4) into the matrix equation

$$\mathbf{L}\mathbf{u} = \mathbf{f}, \quad (7)$$

where \mathbf{u} and \mathbf{f} are the coefficient vectors of u^h and f^h , respectively. The matrix \mathbf{L} is the finite-dimensional approximation of the operator \mathcal{L} , whose resolution depends on the number N of relevant scattering harmonics, and it can be adjusted by varying the scatterer size and/or its complexity. The scatterer is engineered to map the response of Eq. (7) into its scattering matrix, such that the solution u^h is imprinted into the scattered field through $\mathbf{d}^+ = \mathbf{u}$ when the scatterer is illuminated by the converging wave $\mathbf{d}^- = \mathbf{f}$. Hence, the target scattering matrix $\mathbf{S}^{\text{target}}$ mapping the kernel operator of interest into our nonlocal scatterer is defined by

$$\mathbf{S}^{\text{target}}\mathbf{L} = \mathbf{L}\mathbf{S}^{\text{target}} = \mathbf{I}, \quad (8)$$

where \mathbf{I} is the identity matrix. In practice, we may also introduce a scaling factor α in this relation, such that $\mathbf{S}^{\text{target}}\mathbf{L} = \mathbf{L}\mathbf{S}^{\text{target}} = \alpha^{-1}\mathbf{I}$. Relying on the linearity of the problem, this scaling factor is analogous to a preconditioner $\mathbf{P} = \alpha\mathbf{I}$. If we accordingly scale the input function as $\mathbf{d}^- = \alpha\mathbf{f}$, we obtain the same output solution. The factor α introduces an additional degree of freedom to avoid the possible presence of extreme (large or small) entries in the target scattering matrix, which would be associated with resonant features. In Ref. [27], we further discuss the role of α , and we demonstrate how its proper choice can largely enhance the robustness of our operation.

We cast the scatterer design as a partial differential equation (PDE)-constrained optimization problem, where the objective functional M is augmented with the weak form of the governing equation (1) as a PDE constraint. The quality of the design is quantified by the objective functional M that measures the columnwise fitness of the relation (8):

$$M = \sum_{j=-N}^N \frac{1}{2} \|\mathbf{L}\mathbf{d}_j^+ - \mathbf{i}_j\|_2^2, \quad (9)$$

where $\|\cdot\|_2$ denotes the Euclidean norm of the subtended quantity, \mathbf{i}_j is the j th column vector of the identity matrix, and each vector \mathbf{d}_j^+ is associated with the unit excitation of the j th mode.

We optimize the spatial distribution of the relative permittivity ε in the scatterer volume in order to minimize the objective functional (9). A binary material profile is desirable for manufacturability, while conventional optimization techniques handle unconstrained continuous variables more efficiently. To balance between the two, we use a quasi-binary parametrization of the design variable [15],

where we introduce an alternative design variable $t(r, \theta)$ to replace ε :

$$\varepsilon(t) = \frac{\varepsilon_H - \varepsilon_L}{2} \left[1 + \tanh \frac{t}{\gamma} \right] + \varepsilon_L, \quad t \in \Re. \quad (10)$$

Here, ε_H and ε_L are two values of ε that enable a binary implementation of our scatterer, and γ controls the smoothness of the transition between the two. The above parametrization is bounded by $\varepsilon \rightarrow \varepsilon^L$ as $t \rightarrow -\infty$ and $\varepsilon \rightarrow \varepsilon^H$ as $t \rightarrow \infty$, and the gradient is larger in the neighborhood of $t = 0$, which helps the inverse problem to converge to a binary profile. We set γ to a large number at the beginning of our search, leading to a smooth material profile; then, we gradually decrease γ to refine the solution to become binary.

The quasi-binary parametrization allows retaining an unconstrained optimization problem at the cost of increased nonlinearity of the Lagrangian [31], where we use the inexact Newton conjugate gradient method [31,32] to find an optimum. In the solution, a matrix-free calculation of an adjoint-based Hessian-vector operation is implemented for computational efficacy. The finite element method is used to model wave propagation, where perfectly matched layers [33,34] are used to surrogate the unbounded domain, and the domain reduction method [35,36] is used to separate incident and scattered fields. An inverse-design code was developed using a parallel numerical library PETSc [37]. Details are further described in the Supplemental Material [27].

As a first example, we engineered our scatterer to solve a Fredholm equation type II, where its operator for $s \in (0, 2\pi)$ reads

$$\mathcal{L}[\cdot] = 4.25[\cdot] - 12.75 \int_0^{2\pi} \kappa(s, \sigma) g(\sigma) [\cdot] d\sigma, \quad (11)$$

$$g(\sigma) = 1 + 0.1i \cos(2\sigma + 1) \quad \text{and} \\ \kappa(s, \sigma) = \begin{cases} \sigma(1 - \frac{s}{2\pi}), & \sigma < s \\ s(1 - \frac{\sigma}{2\pi}), & \sigma > s \end{cases}. \quad (12)$$

We choose the operating frequency $f = 135$ THz, and set the scatterer radius $a = 1 \mu\text{m}$ and the observation contour radius $r_o = 1.6 \mu\text{m}$. We seek a binary material profile with $\varepsilon^L = 1$ and $\varepsilon^H = 12$, corresponding to a scatterer made of patterned silicon. For this design, the number of harmonics relevant to the scattering problem is $2N + 1 = 5$ and $\alpha = 1$.

After optimization, the result of the inverse design is shown in Fig. 2. In Fig. 2(a) we find excellent agreement between all the elements of the target and the inverted scattering matrix plotted in the complex plane, indicating that our optimal binary profile, shown in Fig. 2(b), is able to synthesize with great accuracy the kernel operator (11). We assess the performance of the nonlocal scatterer by exciting it with the input function

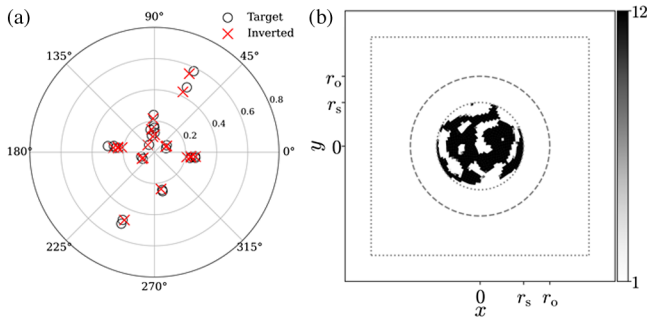


FIG. 2. Inverse-designed nonlocal scatterer to solve a Fredholm equation of type II of choice. (a) Target and inverted scattering matrix elements plotted in the complex plane (here $\alpha = 1$). (b) Inverted relative permittivity profile. The inner dotted curve is the boundary of the control domain, the outer dashed curve represents the observation contour over which the scattered fields are sampled, and the dashed rectangular line represents the PML boundary in our simulations.

$$f(s) = \begin{cases} -0.5 - i, & 0 < s \leq \frac{\pi}{2} \\ 1 + 0.5i, & \frac{\pi}{2} < s \leq \frac{3\pi}{2} \\ -0.3 + 0.3i, & \frac{3\pi}{2} < s < 2\pi \end{cases}. \quad (13)$$

Figures 3(a)–3(b) show the real and the imaginary parts of the incident fields, whereas Figs. 3(d)–3(e) show the corresponding scattered fields from our scatterer. Correspondingly, Fig. 3(c) shows the function f^h sampling the input fields on the observation contour, which represents our input function, and Fig. 3(f) the corresponding solution u^h reconstructed from measuring the scattered fields on the observation contour. The solution u^h is nearly identical to its expected theoretical value u^{ref} , plotted in the same figure, and calculated numerically using Eqs. (11) and (7). Impressively, our nonlocal scatterer is able to calculate with large accuracy the solution of the Fredholm integral equation (11) at the speed of light through its

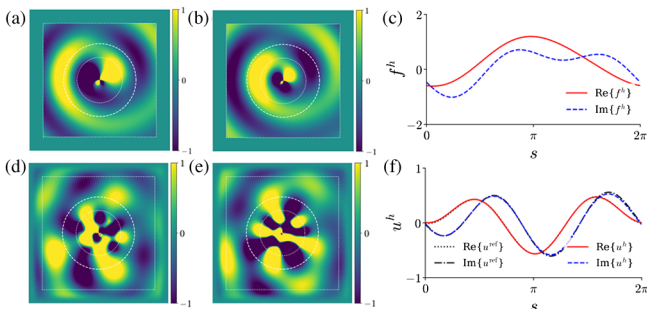


FIG. 3. Wave-based analog computation of Fredholm equation of type II. (a) Real part of the incident field. (b) Imaginary part of the incident field. (c) Real part of the scattered field. (d) Imaginary part of the scattered field. (e) Input function f^h . (f) Solution u^h , reconstructed from the measured \mathbf{d}^+ . The retrieved solution overlaps with the exact value u^{ref} .

complex interaction with the impinging wave describing the input function. By changing the input wave, we can evaluate in real time the corresponding solution simply by observing the scattered fields.

The scatterer nonlocality can also be engineered to solve a differential equation. Figure 4(a) shows the inverted material profile that can solve a second-order differential equation whose linear operator for $s \in (0, 2\pi)$ is

$$\mathcal{L}[\cdot] = \frac{\partial}{\partial s} \left\{ (0.5 \sin s + \sin 2s + 0.3i) \frac{\partial}{\partial s} [\cdot] \right\} + (3 + 0.7i \sin s + 0.3i \sin 2s)[\cdot]. \quad (14)$$

This time, to ensure the robustness and stability of the solution, we chose $\alpha = 0.4$ and used the same material parameters as in the previous example. After optimization, we demonstrate its performance using two different input functions: the same function (13) used in the previous example and another function defined as

$$f(s) = \cos s + \sin 2s + i(\cos s + \cos 2s). \quad (15)$$

The scatterer accurately returns the solution u^h in the scattered field for both excitations, as shown in Figs. 4(b)–4(c), confirming that it correctly maps the kernel operator (14) in its engineered nonlocal interactions. The response does not require sharp resonances through the use of the preconditioner, and therefore it features strong robustness to noise and imperfections. As shown in Fig. 5, the solution indeed maintains excellent quality even when the frequency, the relative permittivity of the scatterer, and the scattered fields are polluted by uniformly

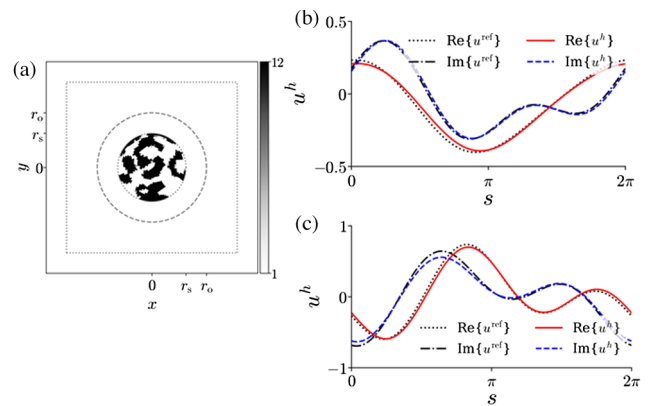


FIG. 4. Inverse-designed nonlocal scatterer to solve a differential equation. (a) Inverted relative permittivity profile. (b) Solution u^h corresponds to the input function (13). (c) Solution u^h corresponds to the input function (15). The retrieved solution shows an excellent agreement with the exact value u^{ref} for both input functions. The inverted scattering matrix, incident wavefield, and scattered wavefield are shown in Ref. [27].

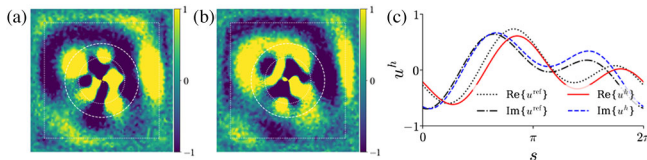


FIG. 5. Solving a differential equation in the presence of noise. A uniformly distributed random noises are added to the frequency (10% of the operating frequency), the relative permittivity of the scatterer (10% of the mean value), and the scattered fields (20% of the mean value). (a) Real part of the scattered field with noise. (b) Imaginary part of the scattered field with noise. (c) Solution u^h reconstructed from the measured \mathbf{d}^+ .

distributed random noises of 10%, 10%, and 20% of their mean values, respectively.

Overall, our results show that engineered scatterers with sizes comparable to the wavelength can operate as efficient wave-based analog computers by engineering their nonlocal response and the coupling among all relevant scattering harmonics. We demonstrated scatterers that can provide solutions to integro-differential equations of choice for arbitrary inputs. This platform can be straightforwardly extended to three-dimensional geometries by extending our formulation to vectorial form, offering even more degrees of freedom for a given scatterer cross-section, and we are currently working towards experimental implementations for acoustic and optical platforms. The computed solution is observed in the scattered fields over an arbitrary contour around the object, so it may be retrieved in the near field or far field of the object. It is not necessary to map the fields over the entire contour, since the number $2N + 1$ of relevant scattering harmonics determines the number of samples that needs to be retrieved around the scatterer to extract the solution of interest, making a practical implementation viable. The resolution of the kernel that can be implemented is fundamentally limited by the number of involved scattering harmonics, which is controlled by the localized near-field variations in the scatterer and its overall size, and it may be enhanced at will by increasing the size of the scatterer, and/or using metamaterial approaches [38], enabling arbitrary complexity of the operator to be synthesized. More complex and ill-behaved operators would lead to larger or more dispersive scatterers. Given the compact and fast nature of the proposed analog computers, we envision cascading multiple of these elements at specific locations to impart more complex operations, or apply a sequence of mathematical operations for unprecedented scalability of the response. Our findings open an exciting paradigm for compact, densely packed analog computing microstructures that can serve as the next generation of compact, low-energy, ultrafast signal processing and equation solving devices for massively parallel computations.

This work was supported by the Air Force Office of Scientific Research MURI program, the Simons Foundation, and the Vannevar Bush Faculty Fellowship.

*To whom correspondence should be addressed.

aalu@gc.cuny.edu

- [1] A. Silva, F. Monticone, G. Castaldi, V. Galdi, A. Alù, and N. Engheta, Performing mathematical operations with metamaterials, *Science* **343**, 160 (2014).
- [2] F. Zangeneh-Nejad, D. L. Sounas, A. Alù, and R. Fleury, Analogue computing with metamaterials, *Nat. Rev. Mater.* **6**, 207 (2021).
- [3] H. Kwon, D. Sounas, A. Cordaro, A. Polman, and A. Alù, Nonlocal Metasurfaces for Optical Signal Processing, *Phys. Rev. Lett.* **121**, 173004 (2018).
- [4] T. Zhu, Y. Zhou, Y. Lou, H. Ye, M. Qiu, Z. Ruan, and S. Fan, Plasmonic computing of spatial differentiation, *Nat. Commun.* **8**, 15391 (2017).
- [5] A. Pors, M. G. Nielsen, and S. I. Bozhevolnyi, Analog computing using reflective plasmonic metasurfaces, *ACS Photonics* **15**, 791 (2015).
- [6] H. Kwon, A. Cordaro, D. Sounas, A. Polman, and A. Alù, Dual-polarization analog 2D image processing with nonlocal metasurfaces, *ACS Photonics* **7**, 1799 (2020).
- [7] A. Cordaro, H. Kwon, D. Sounas, A. F. Koenderink, A. Alù, and A. Polman, High-index dielectric metasurfaces performing mathematical operations, *Nano Lett.* **19**, 8418 (2019).
- [8] S. Zuo, Q. Wei, Y. Tian, Y. Cheng, and X. Liu, Acoustic analog computing system based on labyrinthine metasurfaces, *Sci. Rep.* **8**, 10103 (2018).
- [9] F. Zangeneh-Nejad and R. Fleury, Performing mathematical operations using high-index acoustic metamaterials, *New J. Phys.* **20**, 073001 (2018).
- [10] S.-Y. Zuo, Y. Tian, Q. Wei, Y. Cheng, and X.-J. Liu, Acoustic analog computing based on a reflective metasurface with decoupled modulation of phase and amplitude, *J. Appl. Phys.* **123**, 091704 (2018).
- [11] F. Zangeneh-Nejad and R. Fleury, Topological analog signal processing, *Nat. Commun.* **10**, 2058 (2019).
- [12] W. Zhang and X. Zhang, Backscattering-Immune Computing of Spatial Differentiation by Nonreciprocal Plasmonics, *Phys. Rev. Appl.* **11**, 054033 (2019).
- [13] N. M. Estakhri, B. Edwards, and N. Engheta, Inverse-designed metastructures that solve equations, *Science* **363**, 1333 (2019).
- [14] W. Zhang, C. Qu, and X. Zhang, Solving constant-coefficient differential equations with dielectric metamaterials, *J. Opt.* **18**, 075102 (2016).
- [15] A. Cordaro, B. Edwards, V. Nikkhah, A. Alù, A. Polman, and N. Engheta, Inverse designed metagratings for far-field integral equations solving, in *Conference on Lasers and Electro-Optics*, Washington, DC, (2020), p. FW4B.3, [10.1364/CLEO_QELS.2020.FW4B.3](https://doi.org/10.1364/CLEO_QELS.2020.FW4B.3).
- [16] G. A. Barrios, J. C. Retamal, E. Solano, and M. Sanz, Analog simulator of integro-differential equations with classical memristors, *Sci. Rep.* **9**, 12928 (2019).
- [17] T. W. Hughes, I. A. D. Williamson, M. Minkov, and S. Fan, Wave physics as an analog recurrent neural network, *Sci. Adv.* **5**, eaay6946 (2019).
- [18] C. M. Lalau-Keraly, S. Bhargava, O. D. Miller, and E. Yablonovitch, Adjoint shape optimization applied to electromagnetic design, *Opt. Express* **21**, 21693 (2013).

- [19] D. Sell, J. Yang, S. Doshay, R. Yang, and J. A. Fan, Large-angle, multifunctional metagratings based on freeform multimode geometries, *Nano Lett.* **17**, 3752 (2017).
- [20] Y. Chen, F. Meng, B. Jia, G. Li, and X. Huang, Inverse design of photonic topological insulators with extra-wide bandgaps, *Phys. Status Solidi RRL—Rapid Res. Lett.* **13**, 1900175 (2019).
- [21] H. Goh and L. F. Kallivokas, Inverse metamaterial design for controlling band gaps in scalar wave problems, *Wave Motion* **88**, 85 (2019).
- [22] H. Goh and L. F. Kallivokas, Group velocity-driven inverse metamaterial design, *J. Eng. Mech.* **145**, 04019094 (2019).
- [23] K. Y. Yang, J. Skarda, M. Cotrufo, A. Dutt, G. H. Ahn, M. Sawaby, D. Verduyck, A. Arbabian, S. Fan, A. Alù, and J. Vučković, Inverse-designed non-reciprocal pulse router for chip-based LiDAR, *Nat. Photonics* **14**, 369 (2020).
- [24] W. Jin, W. Li, M. Orenstein, and S. Fan, Inverse design of lightweight broadband reflector for relativistic lightsail propulsion, *ACS Photonics* **7**, 2350 (2020).
- [25] H. Goh and L. F. Kallivokas, Inverse band gap design of elastic metamaterials for P and SV wave control, *Comput. Methods Appl. Mech. Eng.* **370**, 113263 (2020).
- [26] C. F. Bohren and D. R. Huffman, *Absorption and Scattering of Light by Small Particles* (Wiley, Germany, 2008).
- [27] See Supplemental Material at <http://link.aps.org/supplemental/10.1103/PhysRevLett.128.073201> for the numerical modeling of the inverse design problem with its solution method and provides additional figures supporting the examples in the main text. Additional details on scaling factor and an alternative definition of scattering matrix are provided.
- [28] C. F. Sieck, A. Alù, and M. R. Haberman, Origins of Willis coupling and acoustic bianisotropy in acoustic metamaterials through source-driven homogenization, *Phys. Rev. B* **96**, 104303 (2017).
- [29] Y. Liu, Z. Liang, J. Zhu, L. Xia, O. Mondain-Monval, T. Brunet, A. Alù, and J. Li, Willis Metamaterial on a Structured Beam, *Phys. Rev. X* **9**, 011040 (2019).
- [30] L. Quan, Y. Radi, D. L. Sounas, and A. Alù, Maximum Willis Coupling in Acoustic Scatterers, *Phys. Rev. Lett.* **120**, 254301 (2018).
- [31] N. Petra and G. Stadler, Model variational inverse problems governed by partial differential equations, Technical Report No. 11-05, The Institute for Computational Engineering and Sciences, The University of Texas at Austin, 2011, <https://oden.utexas.edu/research/publications?searchNeedle=Model%20variational%20inverse%20problems%20governed%20by%20partial%20differential%20equations>.
- [32] I. Epanomeritakis, V. Akçelik, O. Ghattas, and J. Bielak, A Newton-CG method for large-scale three-dimensional elastic full-waveform seismic inversion, *Inverse Probl.* **24**, 034015 (2008).
- [33] W. C. Chew and W. H. Weedon, A 3D perfectly matched medium from modified Maxwell's equations with stretched coordinates, *Microwave Opt. Technol. Lett.* **7**, 599 (1994).
- [34] S. François, H. Goh, and L. F. Kallivokas, Non-convolutional second-order complex-frequency-shifted perfectly matched layers for transient elastic wave propagation, *Comput. Methods Appl. Mech. Eng.* **377**, 113704 (2021).
- [35] J. Bielak and P. Christiano, On the effective seismic input for non-linear soil-structure interaction systems, *Earthquake Eng. Struct. Dyn.* **12**, 107 (1984).
- [36] B. Poursartip, A. Fathi, and L. F. Kallivokas, Seismic wave amplification by topographic features: A parametric study, *Soil Dyn. Earthq. Eng.* **92**, 503 (2017).
- [37] The PETSc Development Team, PETSc Users Manual, Argonne National Laboratory, ANL-95/11-Revision 3.14.4, 2021.
- [38] A. Alù and N. Engheta, Enhanced directivity from sub-wavelength infrared/optical nano-antennas loaded with plasmonic materials or metamaterials, *IEEE Trans. Antennas Propag.* **55**, 3027 (2007).